Lab on a Chip

PAPER

View Article Online
View Journal | View Issue

Cite this: *Lab Chip*, 2019, **19**, 1736

Integrated inertial-impedance cytometry for rapid label-free leukocyte isolation and profiling of neutrophil extracellular traps (NETs)†

Chayakorn Petchakup, [a] Hui Min Tay,[a] King Ho Holden Li[a] and Han Wei Hou *[ab]

Circulating leukocytes are indispensable components of the immune system, and rapid analysis of their native state or functionalities can help to unravel their pathophysiological roles and identify novel prognostic biomarkers in health and diseases. Herein we report a novel high throughput "sample-in-answer-out" integrated platform for continuous leukocyte sorting and single-cell electrical profiling in a label-free manner. The multi-staged platform enables isolation of neutrophils and monocytes from diluted or lysed blood samples directly within minutes based on Dean flow fractionation (DFF) (stage 1). Next DFF-purified leukocytes are inertially focused in serpentine channels into a single stream (stage 2) prior to impedance detection (stage 3). As a proof-of-concept for neutrophil functional characterization towards diabetes testing, we characterized the formation of neutrophil extracellular traps (NETosis) of healthy and glucose-treated neutrophils and observed significant changes in dielectric properties (size and opacity) between both groups. Interestingly, the NETosis profiles induced by calcium ionophore (Cal) and phorbol 12-myristate 13-acetate (PMA) were also electrically different, which could be attributed to the differential rates of cell enlargement and attenuated membrane permeability. Taken together, these results clearly demonstrated the potential of the developed platform for rapid (~mins) and label-free leukocyte profiling and the use of impedance signatures as novel functional biomarkers for point-of-care testing in diabetes.

Received 14th March 2019,
Accepted 12th April 2019

DOI: 10.1039/c9lc00250b

rsc.li/loc

Introduction

Circulating leukocytes are known to orchestrate various biological processes either as a part of host defense mechanisms or in pathogenesis of major diseases such as cancer, HIV, diabetes mellitus or cardiovascular diseases.[1] Neutrophils are the key effector cells of the innate immunity, and formation of neutrophil extracellular traps (NETosis) is a new defense function to resolve an inflammation by releasing DNA web-like structures composed of decondensed chromatin, histones and granule proteins to trap and kill pathogens.[2–4] NETosis can also contribute to disease development (*e.g.* cancer) and host tissue damage in diabetes mellitus,[5–7] and NETs have been proposed as novel prognostics markers or drug targets.[8,9] As most NETosis assays are based on ELISA[10] or immunofluorescence[11] with a bulk-measurement readout, a better understanding of NETosis-induced biophysical and dielectric changes at single-cell resolution can potentially be exploited for the development of novel diagnostics or immune risk stratification strategies. Conventional fluorescence- and magnetic-activated cell sorting (FACS, MACS) methods are commonly used for leukocyte separation in research settings, but they require antibody labeling which is expensive and time consuming. Our group has previously reported a spiral microfluidic device (Dean flow fractionation, DFF) for size-based leukocyte fractionation.[12,13] By exploiting the presence of inertial focusing-coupled Dean flow in the spiral channel, particles/cells experience size-dependent hydrodynamic forces and migrate to different lateral positions based on their size. This enables continuous size-based cell separation in a high throughput manner (~10^{4-6} cells per min).

For label-free cell measurements, electrorotation and impedance spectroscopy are attractive techniques which characterize the intrinsic dielectric properties of single cells.[14] These techniques have been widely used for leukocyte studies including cell identification,[15–17] leukocyte activation,[18,19] and study of immune functions (NETosis).[20,21] However, impedance cytometry to date has limited clinical utility due to its low flow rate operation and inability to handle complex biosamples (*e.g.* blood) directly.[14,22,23] One key concern is the presence of RBCs and platelets which can co-flow with leukocytes through the detection region simultaneously, thereby causing error in the impedance readout and complicating

[a] *School of Mechanical and Aerospace Engineering, Nanyang Technological University, 50 Nanyang Avenue, Block N3, 639798 Singapore. E-mail: hwhou@ntu.edu.sg; Tel: +6567904950*
[b] *Lee Kong Chian School of Medicine, Nanyang Technological University, 11 Mandalay Road, Clinical Sciences Building Level 11, 308232 Singapore*
† Electronic supplementary information (ESI) available. See DOI: 10.1039/c9lc00250b

signal analysis. Hence, there exists a critical need to develop impedance biosensing platforms with leukocyte sorting capabilities to facilitate assay automation and point-of-care testing. A few notable examples include recent work from Bashir *et al.*[15,24] and Han *et al.*[25,26] for CD4+ cell counting and circulating tumor cell (CTC) analysis, respectively. A major limitation remains in the use of antibodies to isolate specific target cells which can complicate device operation and increase assay cost.

Herein, we report a novel integrated platform combining spiral inertial microfluidics (DFF) and impedance cytometry for continuous, label-free leukocyte sorting and single-cell electrical profiling (Fig. 1). Neutrophils or monocytes are first isolated directly from blood samples using DFF (stage 1), and the DFF-purified leukocytes are subsequently inertially focused in asymmetric serpentine channels into a single stream (stage 2) prior to impedance detection (stage 3). By accounting for the flow rate mismatch between each stage using asymmetric serpentine structures, the developed "sample-in-answer-out" platform facilitates single-step user operation with a rapid readout (<5 min). We first demonstrated neutrophil and monocyte isolation from various minimally processed blood samples, including lysed blood, diluted blood or peripheral blood mononuclear cells (PBMCs), and impedance-based leukocyte enumeration using our platform. As a proof-of-concept for diabetes testing, we measured the NETosis profiles of healthy and glucose-treated neutrophils and observed significant changes in the dielectric properties (size and opacity) between both groups. A comparative study of NETosis induced by calcium ionophore (CaI) and

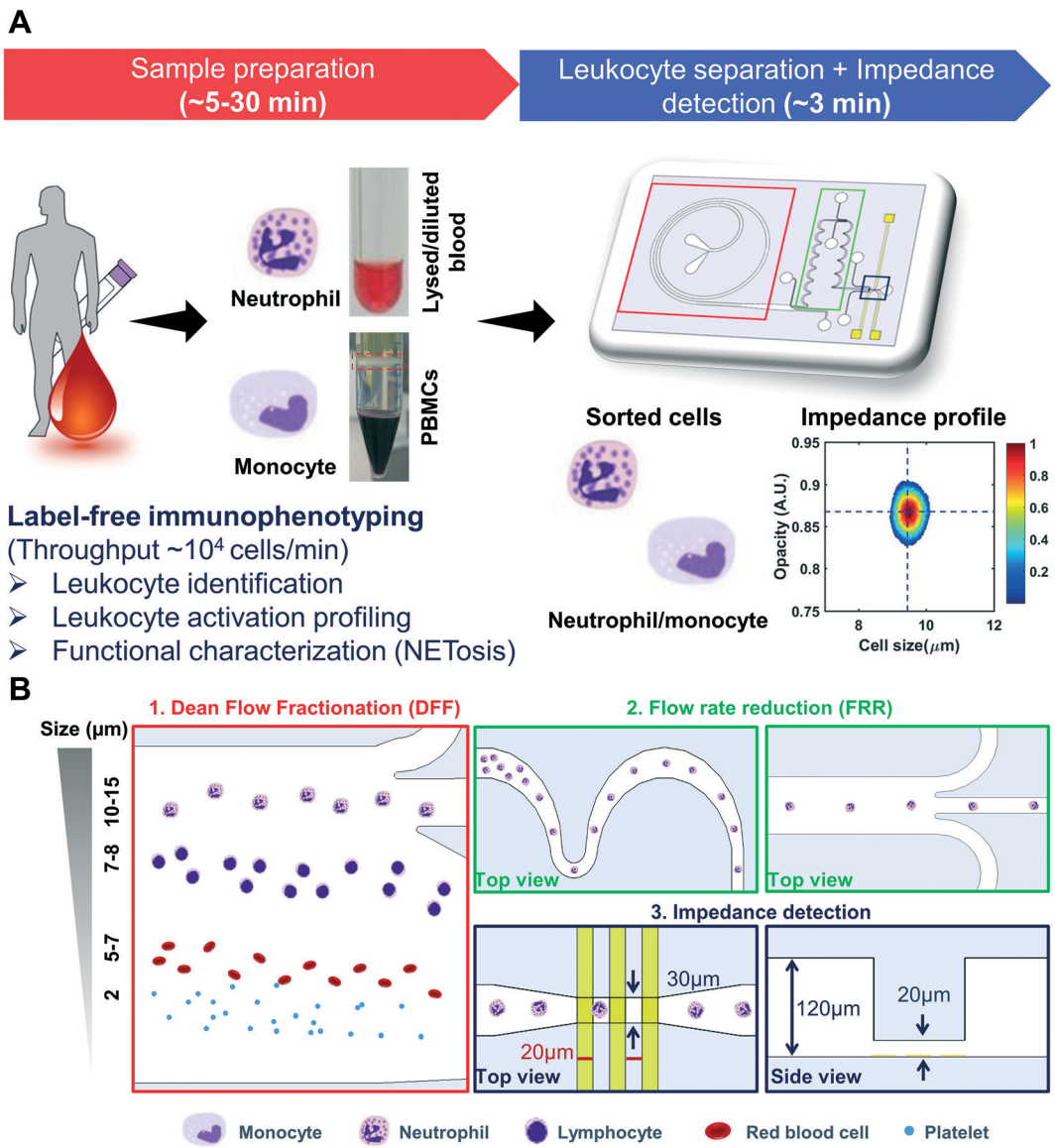

Fig. 1 Integrated platform for leukocyte subset sorting and impedance phenotyping: (A) workflow of the integrated device. Different colored boxes highlight different stages namely the particle sorting (DFF) (stage 1, red), flow rate reduction (FRR) (stage 2, green), and impedance detection (stage 3, blue); (B) schematic illustrations depicting target cell flow behavior at different stages.

phorbol 12-myristate 13-acetate (PMA) using immunostaining, fluorescence spectroscopy and our impedance biosensor further revealed that the dielectric changes are dependent on the NETosis stimulus and could be attributed to the differential rates of cell enlargement and attenuated membrane permeability. Taken together, our results clearly demonstrated the potential of the developed platform for high throughput ($\sim 10^4$ cells per min), single-step and label-free leukocyte profiling in clinical settings and the use of impedance signatures as novel functional biomarkers for point-of-care testing in diabetes and other inflammatory diseases.

Experimental section

Device design and operation

The two-layer integrated platform was fabricated in polydimethylsiloxane (PDMS) using standard soft lithography techniques (see the ESI† for more details). For cell separation, the spiral microchannel (500 μm (w) × 115 μm (h)) has a radius of 0.9–1 cm with a total length of 7–8 cm. For stage 2, the flow rate reduction (FRR) region consists of small curved channels (60–150 μm (w) × 115 μm (h)) and big curved channels (100–300 μm (w) × 115 μm (h)). The height for both stages was chosen to comply with the inertial focusing criterion ($a_p/h > 0.07$ where a_p is the particle size) for leukocytes (~10–15 μm) but not the smaller RBCs (~6–8 μm) and platelets (2 μm). Lastly, the impedance detector (stage 3) with a stepped decrease in channel height (30 μm (w) × 20 μm (h)) is comparable to the target cell size to maximize signal sensitivity for optimal single-cell impedance measurement with coplanar electrodes (30 μm (w) and 20 μm (gap)).

Prior to any experiment, the device was primed with 1% bovine serum albumin (BSA, Biowest) in phosphate buffered saline (PBS, Lonza) for at least 1 h to prevent non-specific adhesion to the device. The sample and sheath were loaded into the outer wall inlet and inner wall inlet, respectively, and perfused at a flow rate ratio of 1 : 10 using syringe pumps (PHD ULTRA™, Harvard Apparatus). Before any measurement or imaging, the platform was allowed to run for 1 min to reach a stabilized state. During experiments, the platform was mounted on an inverted microscope (Nikon Eclipse Ti). Fluorescence images and high-speed images were taken using a Hamamatsu ORCA-Flash4.0 and Phantom V9.1, respectively.

Sample preparation

Depending on the leukocyte of interest, the whole blood samples were pre-processed differently. For neutrophil isolation from lysed blood, RBC lysis buffer (eBioscience) was added into whole blood (10 : 1 v/v) for 3 min and quenched with 0.5% BSA in PBS. For neutrophil isolation from diluted blood, whole blood was diluted in 0.1% BSA in PBS (1 : 500). To acquire peripheral blood mononuclear cells (PBMCs) for monocyte isolation, whole blood was subjected to Ficoll-Paque™ Plus (GE Healthcare) density centrifugation according to the manufacturer's protocol. For impedance measurement, 10 μm fluorescein isothiocyanate (FITC) beads (Polysciences) were added to every sample at 1–2.5 × 10^4 beads per mL. Since the beads have consistent dielectric properties, they will serve as a reference for comparison across different experiments and devices.

Neutrophil treatment for NETosis studies

To study NETosis, neutrophils from lysed blood were prepared from 1 mL of whole blood. After washing twice, the sample were treated with CaI (Sigma-Aldrich, 20 μM) or PMA (Sigma-Aldrich, 2 μM) and incubated at 37 °C. The neutrophils undergoing NETosis were sampled for impedance measurement at various time points: 30 min, 60 min and 120 min. For glucose-treated samples, whole blood was treated with 30 mM D-glucose (Sigma-Aldrich) for 4 h at room temperature prior to RBC lysis.

Imaging of NETosis progression

For nucleus visualization, DFF-isolated neutrophils were stained with Hoechst 33342 dye (Life Technologies) for 15 min at 4 °C. Following washing, cells (~10^4 cells per 50 μL) were seeded in a 5 mm PDMS well coated with poly-L-lysine (Sigma-Aldrich, 0.01% w/v), and SYTOX green nucleic acid stain (500 nM, ThermoFisher Scientific) was added into the well. The fluorescence images of unstimulated neutrophils were taken at 0 min. After that, the NET stimulus (20 μM CaI or 2 μM PMA) was added and images were taken at different time points (30, 60 and 120 min). During the course of imaging, the setup was mounted on an on-stage incubator at 37 °C.

Quantification of NETosis using a microplate reader

Neutrophils were seeded on a 96-well clear bottom black plate (BD Biosciences) at a concentration of ~10^5 cells per well in 200 μL of media (0.1% BSA in PBS) and stimulated with 20 μM CaI or 1 μM PMA. Unstimulated neutrophils served as negative controls. For each condition, either 500 nM or 1 μM SYTOX green was added to detect DNA release. The progress of NETosis was assessed by measuring the fluorescence of SYTOX green–DNA interactions (excitation = 485 nm, emission = 528 nm) using a microplate reader (BioTek Synergy H1 Hybride multi-mode reader) every 30 min for 120 min after stimulation. Duplicates for each condition were performed.

Flow cytometry analysis

The staining protocols for leukocyte identification are similar as previously described.[18] To characterize neutrophil activation before and after sorting, the samples were stained for 30 min at 4 °C with FITC-labelled anti-human CD11b and allophycocyanin (APC)-labelled anti-human CD66b antibodies. Non-specific antibody binding was examined using the corresponding isotype negative control antibodies. The

cells were washed once prior to flow cytometry analysis. All antibodies were purchased from eBioscience (1 : 20 dilution) and analyzed using a BD LSR Fortessa flow cytometer (BD Biosciences).

Statistical analysis

Paired *t*-tests were used to determine the statistical significance of the difference between two sets of data. $P < 0.05$ was regarded as statistically significant. All analyses were performed using GraphPad Prism V7.0 (GraphPad software).

Study approval

Written informed consent was obtained for all subjects during recruitment. All protocols were approved by the Institutional Review Board of Nanyang Technological University (IRB-2014-04/27 and IRB-2018-10-015-02) and Tan Tock Seng Hospital (2014/00416) in compliance with the Human Biomedical Research Act (Ministry of Health, Singapore). Blood samples were collected from venipuncture into a 4 mL K2 EDTA tube (BD vacutainer) of healthy donors for experiments.

For more information on device fabrication, measurement setup and data presentation, refer to the ESI.†

Results and discussion

Device principle

Fig. 1A shows the integrated platform workflow. The platform consists of three stages namely (1) Dean flow fractionation (DFF), (2) flow rate reduction (FRR), and (3) impedance detection using coplanar electrodes. For cell separation using DFF (stage 1), the sample and sheath buffer were introduced at the outer and inner walls of the channel, respectively, at a sample to sheath flow rate ratio of 1 : 10. As the cells flow through the spiral channel, they undergo lateral migration towards the inner wall due to the presence of the Dean drag force (F_D). Near the inner wall, the larger cells (neutrophils/monocytes) experience additional inertial lift forces (F_L) and equilibrate near the inner wall, while smaller components (lymphocytes, RBCs and platelets) recirculate back to the outer wall to achieve separation (Fig. 1B). The larger leukocytes then continue on to the FRR module (stage 2) where they experience alternating Dean vortices in a serpentine channel and inertially focus into a single stream at the channel centre.[27] This is important as it facilitates removal of excess fluid volume from the side channels to reduce the overall volume flow rate entering the impedance detector (Fig. 1B). Lastly, the target cells will enter the impedance detector and two dielectric characteristics are acquired for each cell: (1) opacity (ratio of impedance response magnitude at 1.7×10^6 Hz ($|Z_{HF}|$) to impedance response magnitude at 0.3×10^6 Hz ($|Z_{LF}|$)) reflecting the electrical properties of the cell membrane and (2) $|Z_{LF}|$ which reflects the cell size.

Device characterization with differently sized beads

To determine the optimal flow rate conditions for leukocyte sorting, 10 μm, 7 μm and 5 μm beads which represent monocytes/neutrophils (~10–12 μm), lymphocytes (~7–8 μm) and RBCs (~5–7 μm), respectively, were used for flow rate characterization. In the optimized sample inlet flow rate range of 150–170 μL min^{-1}, 10 μm beads experienced strong inertial forces ($a_p/h > 0.07$ where a_p is the particle size and h is the height of the channel) and focused near the inner wall. As expected, smaller 7 μm and 5 μm beads ($a_p/h < 0.07$) recirculated towards the outer wall due to the dominant Dean force, which resulted in their separation into the waste outlet (Fig. 2A). Flow rate characterization was also performed for the FRR design, and we showed that a similar flow working rate range of 140–170 μL min^{-1} could successfully focus the 10 μm beads to the center of the channel for efficient fluid removal *via* the side outlets (Fig. S2A and B†).

We next determined the sorting efficiency of the developed platform with a bead mixture (5 μm, 7 μm and 10 μm) using high speed imaging and flow cytometry analysis. The high-speed microscopy images were taken at different sections of the device to show particle focusing streams (Fig. S3A†). Eluent was collected from the impedance outlet for flow cytometry analysis. ~98.9% sorting purity of 10 μm beads was achieved at the impedance outlet at the optimal flow rate of 150–160 μL min^{-1} (Fig. 2D). The sorting efficiency decreased slightly at 170 μL min^{-1} to ~90.3% due to the higher 5 μm bead contamination as they recirculated back to the inner wall. We next evaluated the enrichment ratio (ratio of the sorted target cell concentration to the initial target cell concentration) and found that the 10 μm bead concentration was increased ~3-fold (Fig. S3B†). Taken together, our results clearly indicate that the platform can effectively separate and concentrate the 10 μm beads to the impedance detection region (stage 3) while eliminating smaller beads to the waste during DFF (stage 1).

We also examined the effect of particle concentration ranging from 10^5 to 10^6 beads per mL on the 10 μm bead trajectory at different stages and observed negligible differences in particle focusing at DFF and FRR1 (Fig. S4†). However, at a bead concentration of 10^6 beads per mL, the sorting efficiency was slightly deteriorated in FFR2 as evidenced by shifting of the bead trajectory towards the bottom waste outlet. This would possibly occur as the beads become very concentrated after two stages of FRR (~3× enrichment, thus ~3 × 10^6 beads per mL).

Device characterization with different blood samples

We next characterized the leukocyte isolation efficacy from diluted whole blood. Whole blood samples (stained with anti-human CD66b, CD14 and CD3/19 antibodies, to identify neutrophils, monocytes and lymphocytes, respectively) were diluted 1 : 500 and pumped into the integrated platform at 150–170 μL min^{-1}. The eluent was collected from the impedance outlet for flow cytometric analysis. Fig. 3A shows the

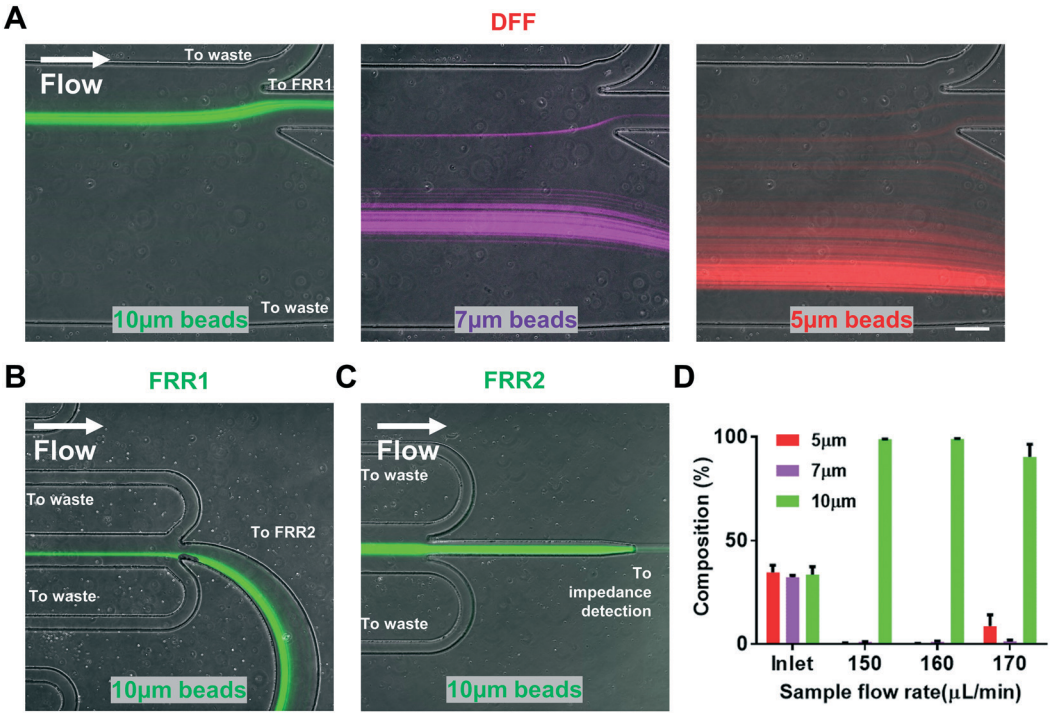

Fig. 2 Device characterization with microbeads at different device stages. (A) Composite fluorescence images of 10 μm (left), 7 μm (center) and 5 μm (right) bead trajectories at the particle sorting stage (DFF). Composite fluorescence images of 10 μm beads at the (B) 1st FRR and (C) 2nd FRR (prior to impedance detection). Scale bar = 100 μm. (D) Sorting purity of 10 μm beads from a mixture of differently sized beads (5 μm, 7 μm and 10 μm). Data are presented as mean ± s.e.m (n = 4).

stacked high-speed microscopy images of the integrated platform at different stages. Due to the high RBC concentration in the inlet sample, a thick RBC band was observed near the outer wall which was similar to the 5 μm bead flow profile. In the FRR stage, DFF-purified leukocytes also focused efficiently to the channel center towards the impedance detector. Based on the flow cytometry analysis, the integrated platform sorting achieved ~80% neutrophil purity with significant lymphocyte and RBC depletion (Fig. 3C). This resulted in an enrichment ratio of ~177-fold due to significant RBC depletion (Fig. S5B and C†). Similar neutrophil sorting performance was also demonstrated using lysed blood samples with a neutrophil purity of >80% (Fig. 3D) and an enrichment ratio of 2.86-fold at the impedance outlet (Fig. S6B†).

Besides neutrophil sorting, we further showed that the device can be used for efficient monocyte isolation from PBMC samples obtained from Ficoll density gradient centrifugation. PBMCs ("buffy coat") primarily consist of lymphocytes, monocytes and platelets as the denser RBCs and granulocytes (neutrophils) would settle at the bottom. PBMC samples were processed under similar flow rate conditions and eluent from the impedance outlet was collected for high speed imaging and flow cytometric analysis. As expected, monocytes equilibrated near the inner wall as they were similar in size to neutrophils, while lymphocytes and platelets were removed into the waste outlet (Fig. 3B). Fig. 3E shows that >80% monocyte sorting purity was achieved for all flow rate conditions tested with a comparable enrichment ratio (~10-fold) at the impedance outlet (Fig. S7B†).

To determine if the developed technology will result in non-specific neutrophil activation during operation, we quantified neutrophil CD66b and CD11b expressions which are reported as activation markers.[28] Negligible differences in both cell markers were observed for healthy (control) and activated (PMA-treated) neutrophils before and after sorting, which was consistent with our previous work,[12] (Fig. 4A). Although cells encounter high shear stresses during flow, the total transit time of the cells inside the device is ~450 ms, which leads to minimal shear-induced effects. The cell viability also remained high (>95%) in post-sorted neutrophils based on trypan blue staining (Fig. S6E†). Taken together, these results clearly indicated the platform versatility in processing different blood samples for gentle and label-free neutrophil and monocyte isolation at high throughput (~10^{4-5} cells per min).

Leukocyte identification and counting using the integrated platform

After optimizing the DFF and FRR stages, we performed impedance measurements of sorted neutrophils and monocytes from lysed blood and PBMCs, respectively. The impedance profile of single cells was plotted as a 2D scatter distribution plot based on the cell size (μm) and opacity ($|Z_{HF}|/|Z_{LF}|$) corresponding to the cell membrane properties.[29,30] See the ESI† for data presentation. Fig. 4B (left) shows a representative impedance profile of sorted neutrophils from lysed blood with

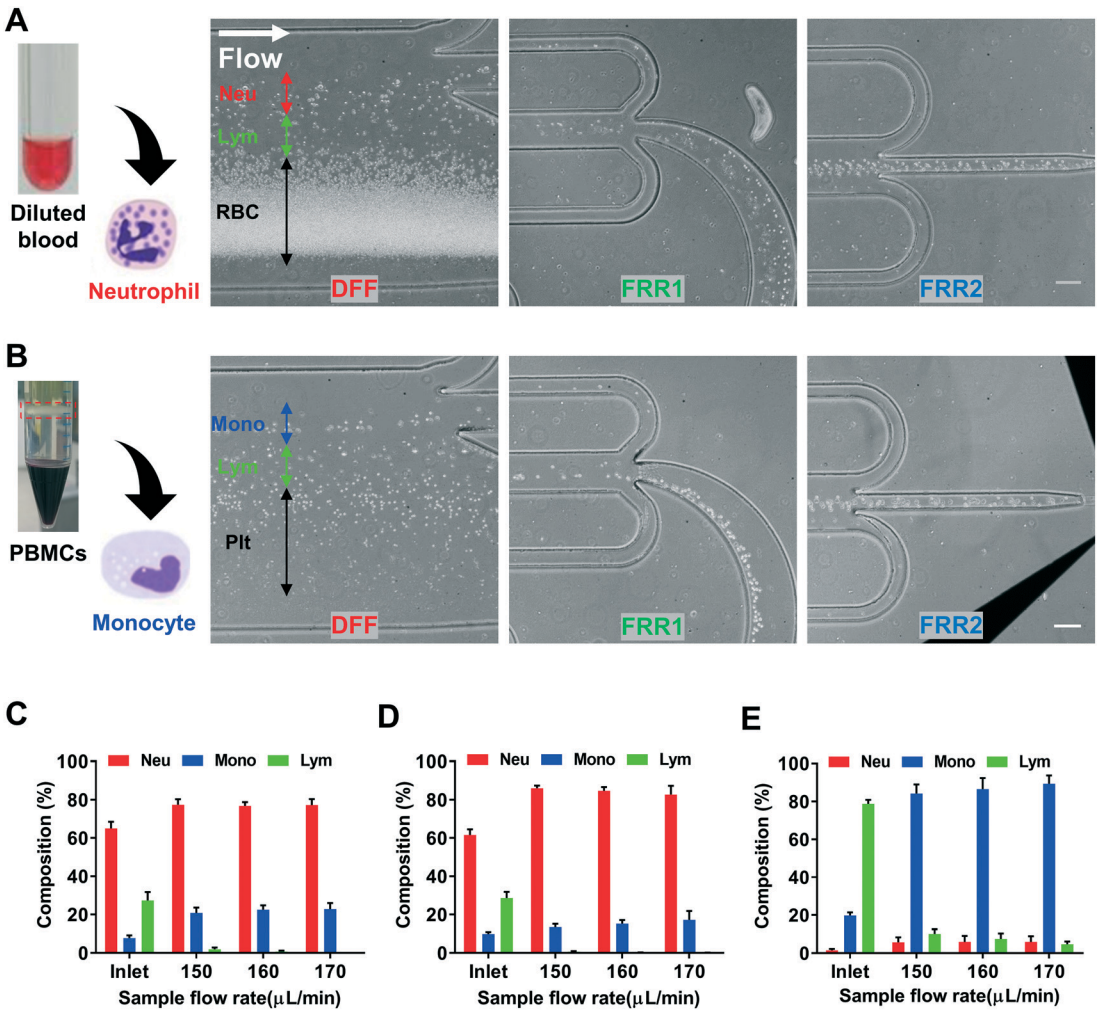

Fig. 3 Device characterization of different blood samples. Composite high speed images of blood cells from (A) diluted blood (1 : 500) (DB) and (B) peripheral blood mononuclear cells (PBMCs) at different device stages. Scale bar = 100 μm. Sorting purity of neutrophils from (C) diluted blood (500×) and (D) lysed blood and (E) monocytes from PBMCs. Data are presented as mean ± s.e.m (n = 4).

dotted lines representing the average or centroid of the population distribution. We then compared the electrical counting using the developed platform with hemocytometer counting and found that our electrical-based leukocyte enumeration was in good agreement with cell counting results over a wide range of cell concentrations (10^{2-5} cells per mL) (Fig. 4B (right)). Monocytes isolated from the PBMC sample were also electrically measured which showed good correlations with hemocytometer counting (Fig. S7D†). Consistent with our previous work,[18] we found that monocytes had a lower opacity than neutrophils due to the subtle size difference which affected the membrane capacitance (opacity $\propto C_{\mathrm{mem}}{}^{-1}$, $C_{\mathrm{mem}} \propto$ surface area).

Additionally, an investigation of the effect of particle concentration on the impedance profile was performed using 10 μm beads. As shown in Fig. S9A,† the cell–cell interspacing below 100 μm indicated that two cells reside within the detection region (100 μm width) and two signals merged together as evidenced in a distorted signal (Fig. S9A† red). It was observed that if the distance between two cells is more than 100 μm, signals become separable without any magnitude distortion (Fig. S9A† green). Therefore, the quantification of the occurrence of cell–cell interspacing less than 100 μm at different concentrations (Fig. S9B†) was performed. At a high sample concentration (10^6 beads per mL), the impedance distribution revealed a higher amount of particles larger than 11 μm (Fig. S9C,† right), which could be due to the presence of two particles between electrode pairs resulting in a superposition of two signals. Hence, the target cell concentration was around 10^5–5×10^5 cells per mL to minimize measurement error.

For impedance throughput, as >80% of beads/cells will enter the impedance detector, the throughput for particle detection will be ~200 beads per s (at 10^6 beads per mL). For a 500× diluted blood sample (whole blood ~5×10^6 WBCs per mL), the diluted cell concentration is 10^4 WBCs per mL. Assuming that ~60% WBCs are neutrophils/monocytes and the separation efficiency is ~80%, the impedance measurement throughput will be ~13 neutrophils per s. A 5 min sample processing of 500× diluted blood will give us ~4000 single cell impedance measurements.

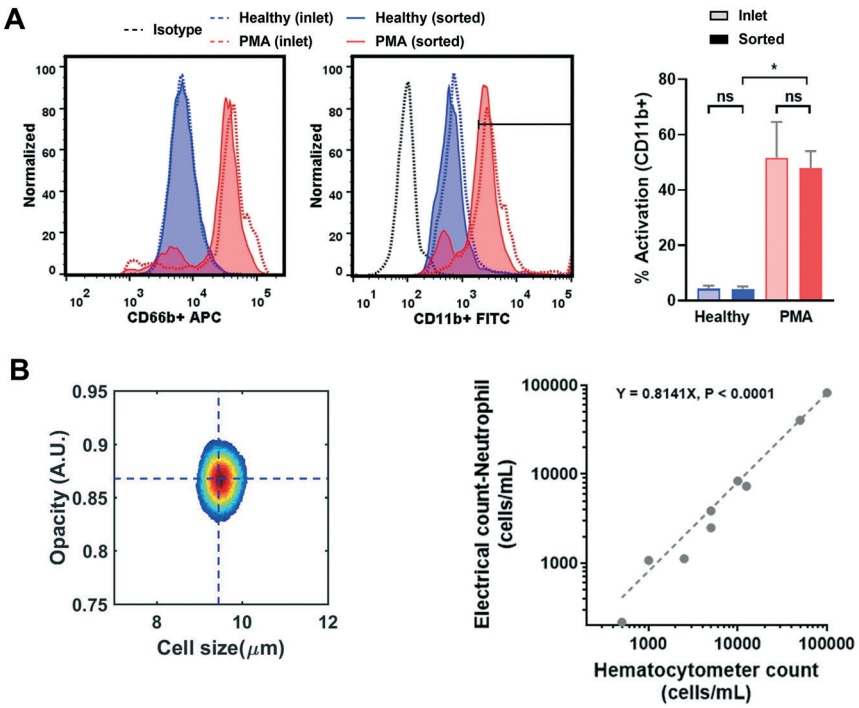

Fig. 4 Leukocyte activation and neutrophil impedance enumeration. Representative flow cytometric analysis of (A) CD66b (left) and CD11b (center) expression of healthy and PMA-treated neutrophils before and after sorting and neutrophil activation (%) quantification based on CD11b (n = 3) (right), *$P \leq 0.05$. (B) Impedance profiling of neutrophils sorted from lysed blood (n = 9517). Dotted lines represent the centroid of the population (left). Comparison of neutrophil enumeration between the integrated platform and hemocytometer (right).

Noteworthily, the high sample flow rate (~140–160 μL min^{-1}) of our device is significantly faster than those of other impedance devices (<50 μL min^{-1}).[16,29] This minimizes cell sedimentation inside the sample syringe and tubing, which is beneficial for cell counting applications as well as processing of rare target cells.

NETosis electrical profiling for functional assessment

To determine if the integrated platform can be used for rapid functional phenotyping, we characterized neutrophils undergoing NETosis induced by calcium ionophore (CaI) as described in Fig. 5A. Neutrophils were stained with Hoechst for nucleus identification and SYTOX green, a cell-impermeant DNA dye. Time-lapse fluorescence imaging was then performed to observe morphological changes during NETosis progression for 120 minutes. As shown in Fig. 5B, the neutrophil size (red dotted lines) and its nucleus became larger with time. The leakage of the nuclear content, due to membrane permeability changes during NETosis, was visualized with the SYTOX green dye after 60 min. We next evaluated the NETosis process using a plate reader and observed a significant increase in the fluorescence signal over time. Glucose-treated neutrophils (30 mM) also exhibited a higher increase in fluorescence intensity as compared to untreated (control) neutrophils, which indicated an upregulation of NETosis (Fig. S10†). We further quantified the NETosis process using our developed impedance cytometer and showed that the opacity and size distribution were higher for neutrophils undergoing NETosis (NET 30 min, 60 min and 120 min) as compared to those of neutrophils without stimulation (control, 0 min) obtained from the same individuals (Fig. 5C). The mean opacity and cell size based on the centroid of the impedance profiles from different donors (n = 5) were quantified and normalized with their respective control (control 0 min) to obtain relative changes. Both the relative opacity and cell size were higher for NETosis neutrophils as compared to those of unstimulated neutrophils (Fig. 5D). These dielectric changes – increase in opacity (increase in impedance response at high frequency) and cell size (increase in impedance response at low frequency) – for neutrophils undergoing NETosis were similar to previous findings by Schröter *et al.* in which they observed elevated magnitude in the impedance spectra.[21] Interestingly, while a larger cell size typically corresponds to a larger surface area and decreased opacity (opacity $\propto C_{mem}^{-1}$, $C_{mem} \propto$ surface area), we observed an increase in opacity for neutrophils undergoing NETosis which could be attributed to changes in the cell membrane or cytoplasm conductivity as CaI induced a massive calcium influx.[31] Griffith *et al.* have also reported that changes in electrorotation spectra of activated neutrophils were due to the expulsion of ions which led to an increase in cell size and reduction of cytoplasm conductivity.[32] Additionally, these dielectric changes could also be associated with nucleus degradation which can be modelled as a structural transformation from a double shelled particle to a single shelled particle. Further studies will be needed to test these hypotheses.

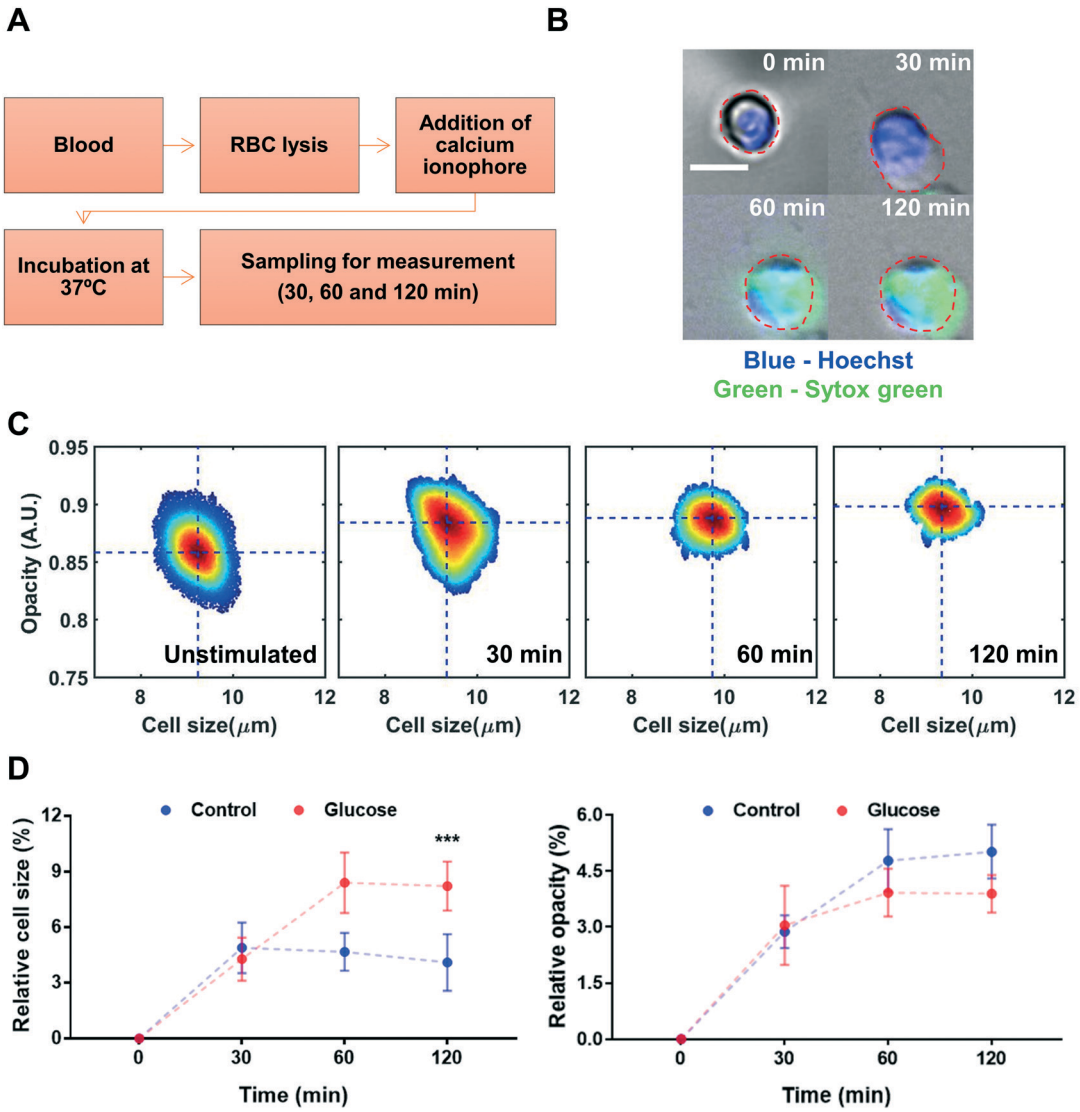

Fig. 5 NETosis profiling using impedance cytometry. (A) Experimental workflow. (B) Overlaid fluorescence (Hoechst and SYTOX Green) and bright-field images showing NETosis progression (using CaI) over the course of 2 hours. Red dotted lines highlight the cell boundary determined from the bright-field images. Scale bar = 10 μm. (C) Representative impedance profiling of neutrophils sorted from lysed blood undergoing NETosis at different time points. Dotted lines indicate the means of each cluster (n = 19 174, 10 957, 4667 and 3813 for unstimulated, NET 30 min, NET 60 min, and NET 120 min, respectively). (D) Average relative neutrophil cell size (left) and opacity (right) with respect to unstimulated neutrophil (0 min) as a control and glucose-treated neutrophil data are presented as mean ± s.e.m (n = 5). ***$P \leq 0.001$.

As a proof-of-concept for diabetes testing, we investigated the influence of glucose treatment on NETosis electrical profiles. Similar trends were observed in the impedance profile of glucose-treated neutrophils undergoing NETosis (Fig. 5D). For both cell size and opacity, there were negligible differences between untreated and glucose-treated neutrophils at the early stage of NETosis (30 min). However, the difference in cell size (glucose > untreated) became significant ($P <$ 0.05) after 60 min and at 120 min. We also observed a slight increase in opacity (untreated > glucose) after 120 min, which could be associated with the larger number of neutrophils undergoing NETosis.[6,33] These impedance results were also consistent with our SYTOX green fluorescence spectrometry which showed higher fluorescence intensities for glucose-treated neutrophils after 60 min (Fig. 5B).

Previous literature studies have reported electrorotation[32] and impedance spectroscopy[21] for NETosis characterization and quantification. However, electrorotation suffers from low throughput (<50 cells per s), and impedance spectroscopy measures the bulk or averaged impedance spectra of neutrophil population undergoing NETosis on interdigitated electrodes. This is a major shortcoming since it is difficult to pinpoint whether the changes in the electrical signal are caused by the released NETs or the structural cellular changes of neutrophils. Additionally, laborious and time-consuming sample preparation processes (Dextran–Ficoll–Lysis, >60 min) were employed for neutrophil isolation.[21] Our developed platform addressed the aforementioned issues by integrating high throughput neutrophil purification and impedance-based NETosis at single-cell resolution within minutes (<5 min).

As NETosis is a time-sensitive cellular function, we used lysed blood samples (containing more neutrophils) to perform rapid impedance measurement (3 min) to prevent the neutrophils from undergoing physical changes during the microfluidic processing. Nevertheless, it is also possible to use diluted blood for NETosis characterization (Fig. S11†). We performed NETosis experiments with diluted blood and a longer measurement time (5 min) to obtain comparable data points with lysed blood samples. The results revealed similar neutrophil impedance profiles and NETosis-induced changes and suggested the feasibility of using diluted blood samples for point-of-care impedance-based NETosis assays.

Critically, a key capability of our integrated platform is the rapid removal of the NETosis stimulus and NETs from purified neutrophils at DFF (stage 1) prior to impedance detection. This on-chip buffer-exchange feature is crucial as additional centrifugation steps to remove the NETosis stimulus may affect the neutrophil phenotype. Although processing of the sample directly without washing is possible, cellular by-products of NETosis (NETs, cell debris, *etc.*) could clog the detection region. Secondly, inertial focusing-based microfluidic modalities (DFF and FFR) enable cell/particle focusing and ordering to facilitate impedance detection.[27] We believe that this novel integration strategy will be generally useful for

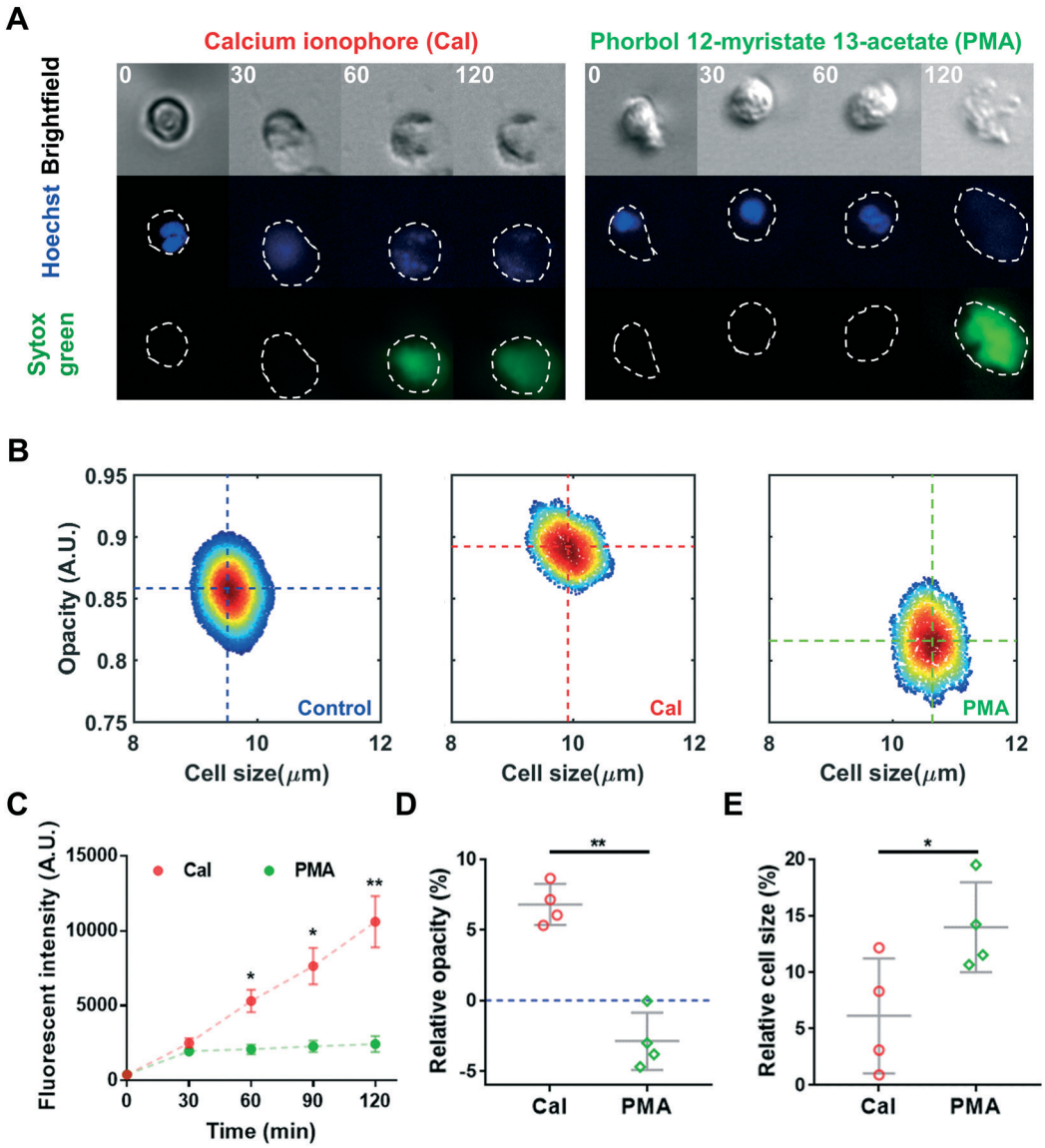

Fig. 6 NETosis impedance profiling with different stimuli. (A) Fluorescence (Hoechst and SYTOX Green) and bright-field images showing NETosis progression *via* Cal (left) and PMA (right) over the course of 2 h. White dotted lines highlight cell boundaries. Scale bar = 10 μm. (B) Representative impedance profiling of unstimulated neutrophils (left, n = 12 660) and neutrophils undergoing NETosis *via* Cal (center, n = 3825) and PMA (right, n = 3424). Dotted lines indicate the centroid of each cluster. (C) Fluorescence intensity profiles of SYTOX green expression for neutrophils undergoing NETosis *via* Cal and PMA for 2 h. Data are presented as mean ± s.e.m. $^*P \leq 0.05$, $^{**}P \leq 0.01$. (D) Average relative neutrophil opacity and (E) cell size with respect to the unstimulated control (0 min). Data are presented as mean ± s.e.m (n = 4). $^*P \leq 0.05$, $^{**}P \leq 0.01$.

researchers who are developing integrated microfluidic platforms.

In future clinical use, both untreated (as a negative control) and treated samples with a specific NETosis stimulus will be measured to study patient-specific NETosis-induced impedance changes. Future work includes increasing of the sample size to study NETosis profiles in healthy individuals and with type 2 diabetes mellitus to design a suitable gating strategy to determine NETosis events in an unknown sample.

Electrical profiling of NETosis by different stimuli

NETosis can be induced by a variety of stimuli such as PMA, CaI and bacteria.[34,35] We next explored whether impedance cytometry can be used to distinguish NETosis induced by different stimuli (CaI and PMA). We first compared the time-lapse fluorescence images of PMA and CaI and observed that CaI induced NETosis more rapidly than PMA, as evidenced in the faster nuclear degradation and an earlier presence of intracellular SYTOX green expression due to the compromised membrane at 60 min (Fig. 6A). The fluorescence spectrometry data also showed that CaI-induced NETosis led to a more rapid and higher SYTOX green expression as compared to PMA (Fig. 6C). The impedance profiles of unstimulated neutrophils and neutrophils undergoing NETosis stimulated by CaI and PMA (120 min) were then characterized using our device (Fig. 6B). Interestingly, the impedance profile of PMA-stimulated neutrophils was opposite to that of CaI-stimulated neutrophils as it shifted towards a lower opacity with a larger cell size difference as compared to the control (unstimulated). The mean opacity and cell size based on the centroid of the impedance distribution were further quantified, and we showed that the relative opacity change was significantly different between both stimuli ($P \leq 0.01$) (Fig. 6D). The change in the cell size was also much larger for PMA ($P \leq 0.05$) (Fig. 6E). Since calcium is required for NETosis,[31] it is likely that CaI and PMA trigger cell membrane dielectric attenuation (and opacity) through calcium ion transport. Cytoplasm conductivity could also be affected as it was reported that CaI resulted in a higher calcium flux and intracellular calcium concentration as compared to PMA.[36] Further studies will be performed to evaluate the observed differences in the dielectric properties between PMA and CaI. Collectively, these results demonstrate that the developed impedance cytometry can be a novel and high throughput single-cell electrical and biophysical characterization tool for NETosis.

This work solely presents the development of an integrated microfluidic device with single-step sample processing to purify and electrically detect neutrophils. This greatly minimizes user sample handling and sample preparation (*e.g.* centrifugation) prior to detection. To facilitate future clinical use, it is necessary to incorporate a microfluidic chip, fluidic pumps and a detection apparatus into a single machine. We envision the developed microfluidic device as a small cartridge which the user will load into the machine prior to sample processing. For data processing, it is currently conducted offline and generally takes about 2–5 min with simple computational tasks such as digital filtering and peak detection. By implementing data processing in embedded systems such as a digital signal processor (DSP) chip or field programmable gate arrays (FPGAs), parallel computing can be exploited to shorten the analysis time tremendously, hence enabling near real time data interpretation.

Conclusion

In summary, we have developed a novel integrated platform for inertial focusing-based cell sorting and electrical phenotyping using impedance cytometry. The "sample-in-answer-out" platform offers great versatility in blood processing and it also significantly minimizes sample handling and user operation. Critically, since both cell sorting and impedance measurement are label-free, the "untouched" sorted cells after impedance measurements can be continuously collected off-chip for downstream assays. Besides leukocyte sorting, identification and counting, the developed platform was used for functional characterization of NETosis in which we observed significant differences in dielectric properties (opacity and size) between healthy and glucose-treated neutrophils, as well as between different NETosis stimuli (CaI and PMA). We envision that our developed platform can be further developed and translated into a point-of-care testing technology for rapid and multi-parametric impedance-based functional immunophenotyping to identify novel biomarkers for disease diagnostics and risk stratification.

Author contributions

C. P, K. H. H. L and H. W. H designed the research. C. P and H. M. T performed the experiments and analyzed the data. C. P, H. M. T and H. W. H wrote the manuscript. All authors reviewed the manuscript.

Conflicts of interest

There are no conflicts of interest to declare.

Acknowledgements

H. W. H would like to acknowledge support from the Singapore Ministry of Education Academic Research Fund Tier 1 (RG53/18), HealthTech NTU-LKCMedicine-NHG POCT (ID POCT/17003) and A. Menarini Biomarkers Pte Ltd. C. P would like to acknowledge support from the NTU Research Scholarship.

References

1 C. Kantari, M. Pederzoli-Ribeil and V. Witko-Sarsat, *Contrib. Microbiol.*, 2008, **15**, 118–146.
2 B. G. Yipp and P. Kubes, *Blood*, 2013, **122**, 2784–2794.
3 V. Brinkmann, U. Reichard, C. Goosmann, B. Fauler, Y. Uhlemann, D. S. Weiss, Y. Weinrauch and A. Zychlinsky, *Science*, 2004, **303**, 1532–1535.

4 V. Papayannopoulos, *Nat. Rev. Immunol.*, 2017, **18**, 134.
5 G. P. Fadini, L. Menegazzo, M. Rigato, V. Scattolini, N. Poncina, A. Bruttocao, S. Ciciliot, F. Mammano, C. D. Ciubotaru, E. Brocco, M. C. Marescotti, R. Cappellari, G. Arrigoni, R. Millioni, S. Vigili de Kreutzenberg, M. Albiero and A. Avogaro, *Diabetes*, 2016, **65**, 1061.
6 S. L. Wong, M. Demers, K. Martinod, M. Gallant, Y. Wang, A. B. Goldfine, C. R. Kahn and D. D. Wagner, *Nat. Med.*, 2015, **21**, 815.
7 S. K. Jorch and P. Kubes, *Nat. Med.*, 2017, **23**, 279.
8 C. Thålin, S. Lundström, C. Seignez, M. Daleskog, A. Lundström, P. Henriksson, T. Helleday, M. Phillipson, H. Wallén and M. Demers, *PLoS One*, 2018, **13**, e0191231.
9 J. Cedervall, Y. Zhang and A.-K. Olsson, *Cancer Res.*, 2016, **76**, 4311.
10 C. Sur Chowdhury, S. Giaglis, U. A. Walker, A. Buser, S. Hahn and P. Hasler, *Arthritis Res. Ther.*, 2014, **16**, R122.
11 T. Hoppenbrouwers, A. S. A. Autar, A. R. Sultan, T. E. Abraham, W. A. van Cappellen, A. B. Houtsmuller, W. J. B. van Wamel, H. M. M. van Beusekom, J. W. van Neck and M. P. M. de Maat, *PLoS One*, 2017, **12**, e0176472.
12 H. W. Hou, C. Petchakup, H. M. Tay, Z. Y. Tam, R. Dalan, D. E. K. Chew, K. H. H. Li and B. O. Boehm, *Sci. Rep.*, 2016, **6**, 29410.
13 H. M. Tay, W. H. Yeap, R. Dalan, S. C. Wong and H. W. Hou, *Anal. Chem.*, 2018, **90**, 14535–14542.
14 C. Petchakup, K. Li and H. Hou, *Micromachines*, 2017, **8**, 87.
15 U. Hassan, N. N. Watkins, B. Reddy Jr, G. Damhorst and R. Bashir, *Nat. Protoc.*, 2016, **11**, 714–726.
16 P. Simon, M. Frankowski, N. Bock and J. Neukammer, *Lab Chip*, 2016, **16**, 2326–2338.
17 H. Song, Y. Wang, J. M. Rosano, B. Prabhakarpandian, C. Garson, K. Pant and E. Lai, *Lab Chip*, 2013, **13**, 2300–2310.
18 C. Petchakup, H. M. Tay, W. H. Yeap, R. Dalan, S. C. Wong, K. H. H. Li and H. W. Hou, *Biosens. Bioelectron.*, 2018, **118**, 195–203.
19 E. Rollo, E. Tenaglia, R. Genolet, E. Bianchi, A. Harari, G. Coukos and C. Guiducci, *Biosens. Bioelectron.*, 2017, **94**, 193–199.
20 G. Urban, J. Wöllenstein, J. Kieninger, A. Schröter, A. Rösen-Wolff and G. Gerlach, *Procedia Eng.*, 2015, **120**, 564–569.
21 A. Schröter, S. Wegner, M. Bulst, H. Parker, A. Rösen-Wolff and G. Gerlach, *Sens. Actuators, B*, 2016, **236**, 947–953.
22 T. Sun and H. Morgan, *Microfluid. Nanofluid.*, 2010, **8**, 423–443.
23 J. Chen, C. Xue, Y. Zhao, D. Chen, M.-H. Wu and J. Wang, *Int. J. Mol. Sci.*, 2015, **16**, 9804.
24 U. Hassan, T. Ghonge, B. Reddy Jr, M. Patel, M. Rappleye, I. Taneja, A. Tanna, R. Healey, N. Manusry, Z. Price, T. Jensen, J. Berger, A. Hasnain, E. Flaugher, S. Liu, B. Davis, J. Kumar, K. White and R. Bashir, *Nat. Commun.*, 2017, **8**, 15949.
25 J. Kim, H. Cho, S.-I. Han and K.-H. Han, *Anal. Chem.*, 2016, **88**, 4857–4863.
26 S.-I. Han and K.-H. Han, *Anal. Chem.*, 2015, **87**, 10585–10592.
27 D. Di Carlo, D. Irimia, R. G. Tompkins and M. Toner, *Proc. Natl. Acad. Sci. U. S. A.*, 2007, **104**, 18892–18897.
28 A. J. van Oostrom, J. P. van Wijk, T. P. Sijmonsma, T. J. Rabelink and M. Castro Cabezas, *Neth. J. Med.*, 2004, **62**, 320–325.
29 D. Holmes, D. Pettigrew, C. H. Reccius, J. D. Gwyer, C. van Berkel, J. Holloway, D. E. Davies and H. Morgan, *Lab Chip*, 2009, **9**, 2881–2889.
30 C. van Berkel, J. D. Gwyer, S. Deane, N. Green, J. Holloway, V. Hollis and H. Morgan, *Lab Chip*, 2011, **11**, 1249–1255.
31 E. F. Kenny, A. Herzig, R. Kruger, A. Muth, S. Mondal, P. R. Thompson, V. Brinkmann, H. V. Bernuth and A. Zychlinsky, *eLife*, 2017, **6**, 24437.
32 A. W. Griffith and J. M. Cooper, *Anal. Chem.*, 1998, **70**, 2607–2612.
33 H. M. Tay, R. Dalan, K. H. H. Li, B. O. Boehm and H. W. Hou, *Small*, 2018, **14**, 1702832.
34 M. F. Konig and F. Andrade, *Front. Immunol.*, 2016, **7**, 461.
35 H. Parker, M. Dragunow, M. B. Hampton, A. J. Kettle and C. C. Winterbourn, *J. Leukocyte Biol.*, 2012, **92**, 841–849.
36 A. K. Gupta, S. Giaglis, P. Hasler and S. Hahn, *PLoS One*, 2014, **9**, e97088.

